Effect of collisional temperature isotropisation on ELM parallel transport in a tokamak scrape-off layer

2016 Plasma Phys. Control. Fusion 58 085004

(http://iopscience.iop.org/0741-3335/58/8/085004)

IOP Publishing Plasma Physics and Controlled Fusion

Plasma Phys. Control. Fusion **58** (2016) 085004 (14pp) doi:10.1088/0741-3335/58/8/085004

Effect of collisional temperature isotropisation on ELM parallel transport in a tokamak scrape-off layer

David Coulette[1], **Sever A Hirstoaga**[2] **and Giovanni Manfredi**[1]

[1] Institut de Physique et Chimie des Matériaux de Strasbourg, CNRS and Université de Strasbourg, BP 43, F-67034 Strasbourg, France
[2] Inria Nancy-Grand Est (TONUS team) and Institut de Recherche en Mathématiques Avancées, Université de Strasbourg, France

E-mail: coulette@unistra.fr, hirstoaga@math.unistra.fr and manfredi@unistra.fr

Received 7 March 2016, revised 17 May 2016
Accepted for publication 8 June 2016
Published 5 July 2016

Abstract

We develop a hybrid model to describe the parallel transport in a tokamak scrape-off layer following an edge-localized mode (ELM) event. The parallel dynamics is treated with a kinetic Vlasov–Poisson model, while the evolution of the perpendicular temperature $T_\perp$ is governed by a fluid equation. The coupling is ensured by isotropising collisions. The model generalises an earlier approach where $T_\perp$ was constant in space and time (Manfredi *et al* 2011 *Plasma Phys. Control. Fusion* **53** 015012). Numerical results show that the main effect comes from electron–electron collisions, which limit the decrease of the parallel electron temperature and increase the potential drop in the Debye sheath in front of the surface. Ion–ion collisions have an almost negligible impact. The net effect is an increased peak power load on the target plates.

Keywords: Vlasov–Poisson, edge localized modes, parallel transport, scrape off layer, tokamaks

(Some figures may appear in colour only in the online journal)

1. Introduction

An outstanding issue in the operation of large tokamak devices such as ITER lies in the high power load deposited on plasma facing components. Violent outbursts of particles and energy in the tokamak edge region—the so-called edge-localized modes (ELMs)—are notably a major concern: the resulting particle and energy fluxes on the plasma-facing components lead to a decrease of their lifetime, as well as an increase of the sputtering yield and emission of high-Z impurities into the plasma [1, 2].

As far as modeling is concerned, the birth and growth of the ELMs are treated using magnetohydrodynamic (MHD) models with realistic magnetic field geometry [3–5]. Once the ELM-driven plasma pulse has crossed the magnetic separatrix, it travels mainly parallel to the magnetic field lines and ends up hitting the divertor plate. Such parallel transport generally occurs over too short time scales (a few hundred microseconds) to ensure the validity of fluid closures (for a detailed comparison between fluid and kinetic results, see [6]). As fully three-dimensional (3D3V) kinetic models with realistic geometry are too complex and numerically costly, several authors have developed more tractable 1D models where only the parallel transport is considered, whereas the transverse dynamics is neglected [7–12]. Such models usually solve the Vlasov kinetic equation along a magnetic field line that connects the divertor plates, although more recently a gyrokinetic approach was also proposed [13].

The simplest kinetic description of parallel transport is the so-called free-streaming model developed by Fundamenski and Pitts [7], for which both the parallel electrostatic field and all collisional processes are neglected. Although somewhat crude, this model has the advantage of providing explicit solutions for the particle and energy fluxes on the walls, which

reproduce with rather good accuracy some of the main features of an ELM signal, most notably its rapid rise ($\sim$200 μs) followed by a much slower decay (up to 3 ms). It has also been shown to be consistent with the low electron temperatures measured at the divertor target of the JET tokamak [14, 15]. Simply put, the free-streaming model describes the evolution of the ion population from a thermal distribution with no drift to a cold beam directly towards the wall. However, it completely neglects the energy transfer from the electron to the ion population through the self-consistent electric field, leading to an underestimation of the peak fluxes on the wall. A large part of this energy transfer occurs during the initial quasi-neutral expansion of the ELM plasma, well before any significant fluxes have reached the divertor plate. Thus, a good approximation for the fluxes on the wall can be obtained by using a modified free-streaming model [12] where the initial ion temperature is replaced by $T_{e0} + T_{i0}$, (or, equivalently, by replacing the ion thermal speed with the sound speed c_{S0}), i.e. by assuming that all the electron energy is transferred to the ions long before a significant fraction of the plasma has reached the wall. This assumption is supported by the relative scaling between the quasi-neutral expansion time $\tau_\sigma = \sigma_0/c_{S0}$ (where σ_0 is the typical parallel extension of the ELM filament) and the transit time towards the target plate $\tau_L = L/c_{S0}$, where L is the distance between the midplane and the plate. It was later shown [11] that as long as $L^\star \equiv L/\sigma_0 = \tau_L/\tau_\sigma$ is large enough (typically above 5) the modified free-streaming model shows excellent agreement with the results of Vlasov–Poisson simulations. Consistently, the sheath forming at the target plate was shown to have a negligible impact, due to the low fraction of electron thermal energy that remains available to form the sheath.

In the above 1D1V models (either Vlasov–Poisson or free-streaming), the parallel and perpendicular dynamics were completely decoupled for both particle species. The perpendicular velocity distributions were assumed to be Maxwellian with constant temperature. The purpose of the present work is to ascertain whether the collision-driven relaxation between the parallel and perpendicular temperatures [16–18] of each species during the ELM propagation can modify the shape of the distribution function and consequently the fluxes reaching the wall.

Recently, numerical simulations of a 1D3V Vlasov–Poisson model including the effect of Coulomb collisions were performed with the particle-in-cell (PIC) code `BIT1` [11]. It was shown that the transfer of electron thermal energy from the perpendicular plane to the parallel direction could indeed impact significantly the energy fluxes of both species. In order to examine these effects more closely, without bearing the cost of a full 1D3V simulation, we propose to extend the 1D1V Vlasov–Poisson model of [10] to include a fluid equation for the evolution of the perpendicular temperature for both species. Such perpendicular temperature is coupled to the parallel transport through a collision operator that models the temperature isotropisation process (i.e. the process through which the parallel and perpendicular temperatures of each particle species equilibrate). The resulting model can be viewed as a hybrid approach where the (fast) parallel transport is modeled kinetically with a Vlasov equation while the (slower) perpendicular processes are described by a fluid equation for the corresponding perpendicular temperature. Hybrid models were used in the past in plasma physics [19], but this is, to the best of our knowledge, their first application to the physics of ELMs.

The description of the model, its numerical implementation, and the simulation parameters are addressed in section 2. In section 3 we show and illustrate the results of numerical simulations of this model in the case of an instantaneous ELM source. The effect of finite pulse duration is examined in section 4, while the general energy transfer dynamics is analysed in section 5. A general discussion is presented in section 6.

2. Parallel transport model with perpendicular temperature

2.1. Physical model

The model used in the present work is an extension of the one developed in [10] and later exploited in [11, 12]. A static and spatially uniform magnetic field $\mathbf{B}$ is oriented along the x axis. The charged particles (or rather, their guiding centres) travel along the magnetic field lines, but not across them. Thus, we can adopt a one-dimensional geometry along the parallel direction. No spatial dependence exists in the transverse coordinates (y, z), so that the probability distribution functions f_s for each particle species s evolve in the 1D3V phase space $(x, \mathbf{v})$. The relevant Vlasov equation in such a phase space is:

$$\partial_t f_s + v_x \partial_x f_s + \frac{q_s}{m_s}(\mathbf{E} + \mathbf{v} \times \mathbf{B}) \cdot \nabla_{\mathbf{v}} f_s = \mathcal{C}_s(f_s) + \mathcal{S}_s, \tag{1}$$

where q_s and m_s are the charge and mass, $\mathbf{E}(t, x) = -\nabla\phi(t, x)$ is the electric field, and ϕ the electric potential. The right-hand side of equation (1) contains collisional and source terms to be discussed below.

For each particle species s the velocity distribution function is assumed to be the product of a parallel distribution $g_s(t, x, v_x)$ and a perpendicular isotropic Maxwellian with no drifts:

$$f_s(t, x, \mathbf{v}) = g_s(t, x, v_x) \frac{m_s}{2\pi T_{\perp,s}(t, x)} \exp\left(-\frac{m_s v_\perp^2}{2T_{\perp,s}(t, x)}\right), \tag{2}$$

where $T_\perp$ is the perpendicular temperature, which depends on both x and t, in contrast to [10] where it was assumed to be constant. With these assumptions, the magnetic term in the Vlasov equation (1) disappears and the electric term reduces to its parallel component $E_x = -\partial_x\phi$. Thus we have

$$\partial_t f_s + v_x \partial_x f_s - \frac{q_s}{m_s} \partial_x\phi(t, x) \partial_{v_x} f_s = \mathcal{C}_s(f_s) + \mathcal{S}_s. \tag{3}$$

This approximation allows us to focus on the perpendicular temperature effects, at the expense of perpendicular fields and drifts, which are neglected here and would require a computationally much more complex 2D model. Finally, the

electrostatic potential is determined self-consistently from Poisson's equation

$$\partial_{xx}\phi = -\frac{1}{\epsilon_0}\sum_s q_s n_s. \tag{4}$$

For the collisions, we use a Bhatnagar–Gross–Krook (BGK) collision operator [20]

$$\mathcal{C}_s(f_s) = \nu_s(f_{\mathrm{Ms}} - f_s), \tag{5}$$

$$f_{\mathrm{Ms}} = n_s\left(\frac{m_s}{2\pi T_s}\right)^{3/2}\exp\left(-\frac{m_s(v_x-u_{xs})^2}{2T_s}\right)\exp\left(-\frac{m_s v_\perp^2}{2T_s}\right), \tag{6}$$

where ν_s is the like-particle relaxation rate (the electron–ion relaxation rate is neglected, as explained in section 2.2). The effect of the BGK term is to drive f_s towards the isotropic Maxwellian $f_{\mathrm{Ms}}(t,x,\mathbf{v})$. The density $n_s = \int f_s \mathrm{d}^3\mathbf{v} = \int g_s \mathrm{d}v_x$, mean velocity $u_{xs} = \int f_s v_x \mathrm{d}^3\mathbf{v}/n_s = \int g_s v_x \mathrm{d}v_x/n_s$, and total temperature $T_s = m_s\int f_s(\mathbf{v}-\mathbf{u}_s)^2\mathrm{d}^3\mathbf{v}/(3n_s)$ are computed self-consistently from the distribution function f_s. Note that only drifts in the parallel direction are allowed, i.e. $\mathbf{u}_{\perp,s} = 0$.

The source term $\mathcal{S}_s$ represents the growth of the ELM event. In all results presented hereafter, it is taken as a separable function of time, space, and velocity coordinates

$$\mathcal{S}_s(t,x,\mathbf{v}) = s(t)N(x)G_s(v_x)H_s(\mathbf{v}_\perp) \tag{7}$$

where

$$N(x) = n_0\exp\left(-\frac{x^2}{2\sigma_0^2}\right), \tag{8}$$

$$G_s(v_x) = \sqrt{\frac{m_s}{2\pi T_{\parallel 0}}}\exp\left(-\frac{m_s v_x^2}{2T_{\parallel 0}}\right), \tag{9}$$

$$H_s(\mathbf{v}_\perp) = \frac{m_s}{2\pi T_{\perp 0}}\exp\left(-\frac{m_s v_\perp^2}{2T_{\perp 0}}\right). \tag{10}$$

In all the following, we assume no temperature anisotropy for the growing ELM, i.e. $T_{\parallel 0} = T_{\perp 0} \equiv T_0 = \text{const.}$. The source temperature is also assumed to be the same for both ions and electrons, so that the corresponding sound speed is $c_{\mathrm{S}0} = \sqrt{2}\,v_{\mathrm{th,i}\,0}$, where $v_{\mathrm{th,i}\,0}$ is the ion thermal speed. The parameter σ_0 determines the extension of the ELM pulse. For the time envelope of the source $s(t)$, we will first (section 3) consider a Dirac pulse $s(t) = \delta(t)$, which is equivalent to simply setting the initial distribution equal to $N(x)G_s(v_x)H_s(\mathbf{v}_\perp)$ and removing the source. Subsequently (section 4) we will study the effect of a time-distributed source with

$$s(t) = Ct^2\exp\left[-\frac{(t-t_0)^2}{2\sigma_t^2}\right], \tag{11}$$

where C is chosen so that $\int_0^\infty s(t)\mathrm{d}t = 1$. The above temporal profile is chosen to model an ELM pulse with a finite duration (roughly, σ_t) that peaks around a certain time (roughly, t_0). The t^2 factor is introduced so that the ELM pulse starts at zero amplitude. This is the same profile that was used in [10], to which we compare the present results. Further, we performed additional simulations (not shown in this paper) using a different profile (step function constant for $t < t_0$ and vanishing for $t > t_0$) and the results were qualitatively similar.

Substituting the Ansatz of equation (2) into equation (3) and integrating over $\mathbf{v}_\perp$ we obtain the evolution equation for the parallel distribution g_s:

$$\partial_t g_s + v_x\partial_x g_s - \frac{q_s}{m_s}\partial_x\phi\partial_{v_x}g_s = \nu_s(g_{\mathrm{Ms}} - g_s) + s(t)N(x)G_s(v_x), \tag{12}$$

where

$$g_{\mathrm{Ms}}(t,x,v_x) = \int f_{\mathrm{Ms}}\mathrm{d}^2\mathbf{v}_\perp = n_s\left(\frac{m_s}{2\pi T_s}\right)^{1/2}\exp\left(-\frac{m_s(v_x-u_{xs})^2}{2T_s}\right). \tag{13}$$

Taking the second order moment in $v_\perp$ of equation (3), we obtain the evolution equation for $T_{\perp,s}$

$$\partial_t T_{\perp,s} + u_{xs}\partial_x T_{\perp,s} = \frac{\nu_s}{3}(T_{\parallel,s} - T_{\perp,s}) + \frac{s(t)N(x)(T_{\perp 0} - T_{\perp,s})}{n_s(t,x)}, \tag{14}$$

where $T_{\parallel,s} = m_s\int g_s(v_x-u_{xs})^2\mathrm{d}v_x/n_s$. To derive equation (14) we have used the fact that $T_s = \frac{1}{3}(T_{\parallel,s} + 2T_{\perp,s})$ and the continuity equation $\partial_t n_s + \partial_x(n_s u_{xs}) = s(t)N(x)$. The coupling between the parallel and perpendicular dynamics occurs in equation (12) through the total temperature in the parallel BGK operator, and in equation (14) through the quantities n_s, u_{xs}, and $T_{\parallel,s}$, which are moments of the parallel velocity distribution function g_s. Naturally, setting $\nu_s = 0$ we recover the collisionless model of [10], where the parallel and perpendicular motions are completely decoupled. The new terms represent the temperature isotropisation (first term on the right-hand side of equation (14)) and the transport of $T_{\perp,s}$ induced by the parallel fluid velocity u_{xs} (second term on the left-hand side of equation (14)).

2.2. Implementation

The resulting hybrid model is constituted of equations (12)–(14). The corresponding numerical code can be viewed as an extension of the 1D1V kinetic code `VESPA` [10], which solves the Vlasov–Poisson system on a fixed phase-space grid using a finite-volume scheme [21]. The specificity of the `VESPA` code is that it is *asymptotic-preserving* in the small dimensionless parameter $\lambda = \lambda_{\mathrm{D}}/L$, where λ_{D} is the Debye length. In suitable dimensionless units, the Poisson equation (4) can be written as

$$\lambda^{-2}\partial_{xx}\phi = n_e - n_i, \tag{15}$$

and becomes singular when $\lambda \to 0$. In the simulations, this fact requires that the grid spacing and the time step be smaller

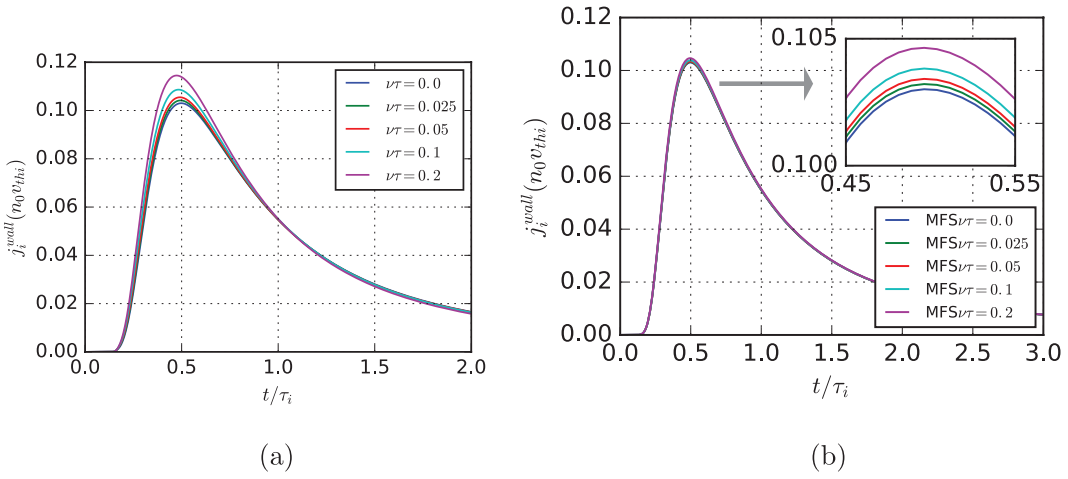

Figure 1. Temporal evolution of the ion particle fluxes at the right wall ($x = L$), for different collisionalities: (a) numerical results; (b) modified ($v_{\mathrm{th,i}\,0} \to c_{\mathrm{S}0}$) free-streaming model with first order ion–ion collisional corrections (see the appendix). (a) H^+, (b) H^+ free-streaming.

than, respectively, the Debye length and the inverse plasma frequency—a rather constraining condition. The asymptotic-preserving technique reformulates Poisson's equation in a way that is not singular, and thus lifts the above constraints on the numerical resolution [10]. Here, we take $\lambda = 10^{-3}$, which is still larger than the realistic value for tokamaks, $\lambda \approx 10^{-5}$–10^{-6}. However, as was shown in [10] all the qualitative features of the ELM propagation are already recovered for the value of λ used in this work.

The additional transport equation (14) for the perpendicular temperature is solved with an upwind finite-volume method [22] improved by using high-resolution corrections. Even though this scheme is formally first-order accurate in space and time, in practice it works much better than the second-order Lax–Wendroff method, since a minmod limiter is used to avoid spurious spatial oscillations. The time step is variable in order to guarantee that the Courant–Friedrichs–Lewy (CFL) condition $|u_x|\Delta t < \Delta x$ is always satisfied.

Equations (12)–(14) are solved on an interval $x \in [-L, L]$, where $x = \pm L$ represent the locations of the target plates. We take $L = 1000\lambda_{\mathrm{D}}$, where $\lambda_{\mathrm{D}} = \sqrt{\epsilon_0 T_0/(n_0 e^2)}$ is computed with the source parameters. For each species the velocity space grid spans the range $[-6v_{\mathrm{th},s}, 6v_{\mathrm{th},s}]$. The resolution is $N_x = 2000$ and $N_v = 1000$ points in position and velocity space respectively. The time step varies between one-half and four times the inverse plasma frequency. As to the boundary conditions, the plates are supposed to be perfectly absorbing surfaces (i.e. the incoming flux is zero) and are kept at constant electric potential $\phi(\pm L) = 0$. The plasma source is centered at $x = 0$, with a characteristic width $\sigma_0 = 0.1L$. We will consider hydrogen ions with $Z = 1$ (so that $q_{\mathrm{i}} = -q_{\mathrm{e}} = e$) and $m_{\mathrm{i}} = 1836 m_{\mathrm{e}}$.

We will be primarily interested in the particles and energy fluxes on the target plates. At the right target ($x = L$), these are defined respectively as

$$j_s(t) = \int v_x f_s(t, L, \mathbf{v}) \mathrm{d}^3\mathbf{v} = \int v_x g_s(t, L, v_x) \mathrm{d}v_x, \qquad (16)$$

$$Q_s(t) = \int \frac{1}{2} m_s (v_x^2 + v_\perp^2) v_x f_s(t, L, \mathbf{v}) \mathrm{d}^3\mathbf{v} = Q_{\parallel,s}(t) + Q_{\perp,s}(t), \qquad (17)$$

where $Q_{\perp,s} = j_s T_{\perp,s}$ and $Q_{\parallel,s} = \int \frac{1}{2} m_s v_x^3 g_s(t, L, v_x) \mathrm{d}v_x$. At the left target ($x = -L$), because of the symmetry, j_s and Q_s are still defined by the above equations but with opposite sign.

As our main objective is to assess the impact of the parallel-perpendicular coupling on the fluxes reaching the target plates, we perform parametric scans in the collision rate ν_s. The values of the collision rates used in the simulations are estimated from the isotropisation rates for the relevant ELM parameters [18]. Following such estimations, the ion and electron collision rates are not set independently but adjusted so that $\nu_{\mathrm{e}}/\nu_{\mathrm{i}} = \sqrt{m_{\mathrm{i}}/m_{\mathrm{e}}}$. As a consequence, noting $\tau_s = L/v_{\mathrm{th},s}$ the transit time for each species[3], the product $\nu_s\tau_s$ is the same for both species and is simply noted $\nu\tau$. This quantity will be used to quantify the amount of collisionality in each numerical simulation.

For a typical plasma with pedestal parameters $T_{\mathrm{e}} = T_{\mathrm{i}} = 1.5$ keV, $n_{\mathrm{e}} = n_{\mathrm{i}} = 5 \times 10^{19}$ m^{-3} and $L = 30$ m, we obtain a value $\nu\tau \approx 0.15$ by following the approach of [18][4]. It must be noted that, with these parameters, one has $\lambda_{\mathrm{D}}/L \approx 10^{-6}$, whereas the value used in our simulations is 1000 times larger. In practice, this amounts to employing a much shorter connection length L while increasing the collision rates $\nu_{\mathrm{e,i}}$ to keep the dimensionless product $\nu\tau$ constant. In the forthcoming simulations, the latter will vary in the range $0 \leqslant \nu\tau \leqslant 0.2$.

The scaling $\nu_{\mathrm{e}} = \nu_{\mathrm{i}}\sqrt{m_{\mathrm{i}}/m_{\mathrm{e}}}$ has a strong impact on the overall dynamics of the collisionless plasma expansion following the ELM event, which is governed by the ion transit time $L/v_{\mathrm{th,i}} = \tau_{\mathrm{i}}$. For the range of $\nu\tau$ values considered here and for the relevant ELM timescale $t_{\mathrm{ELM}} \sim \tau_{\mathrm{i}}$,

[3] Strictly speaking, the transit time is $\tau_L = L/c_{\mathrm{S}0}$, defined with the sound, instead of thermal, speed. However, for the ions, these quantities only differ by a factor of $\sqrt{2}$ when $T_{\mathrm{e}} = T_{\mathrm{i}}$.

[4] Equation (26) in [18] gives the temperature relaxation rate for same-species particles; we used $\ln\Lambda = 15$ for the Coulomb logarithm.

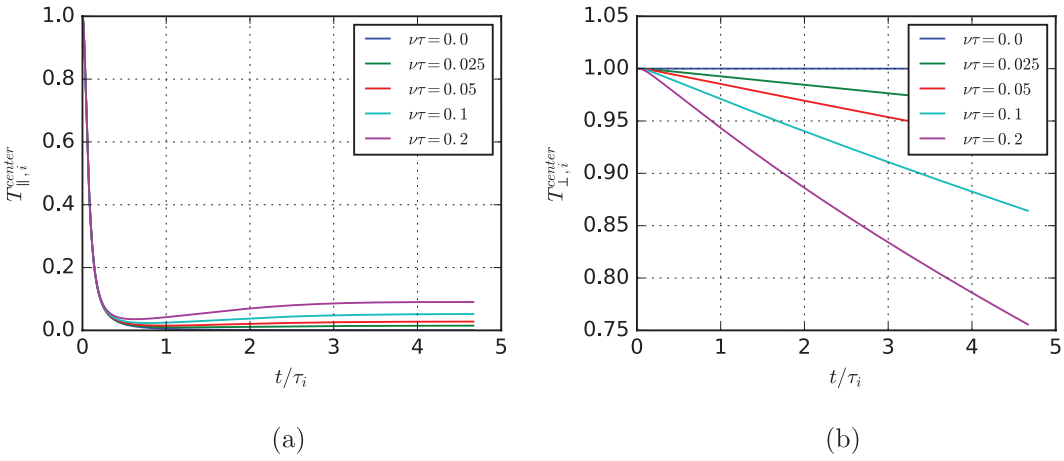

Figure 2. Ion parallel (a) and perpendicular (b) temperatures at $x = 0$, for different collisionalities. (a) H^+. (b) H^+.

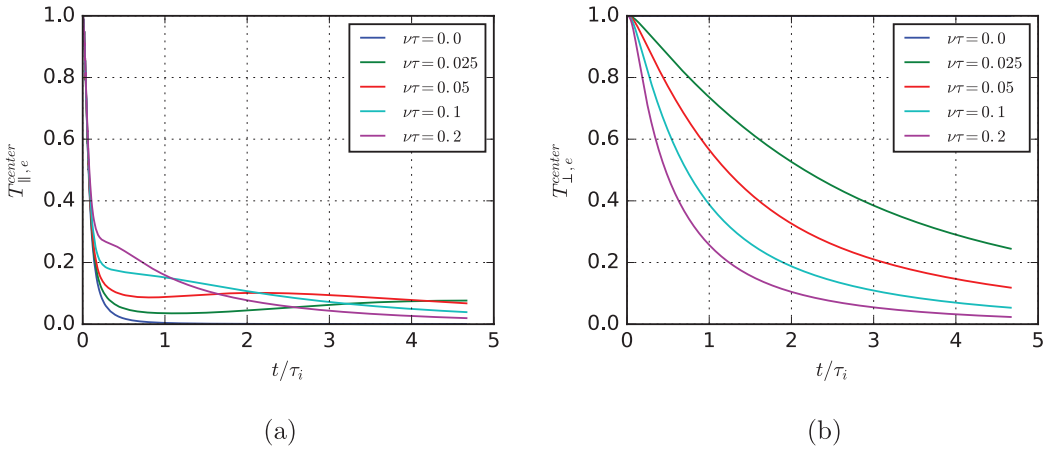

Figure 3. Electron parallel (a) and perpendicular (b) temperatures at $x = 0$. (a) e^-. (b) e^-.

we have that $\nu_i t_{\mathrm{ELM}} \sim \nu_i \tau_i = \nu\tau$ is indeed small, so that the ion collision operator has only a perturbative effect. However, $\nu_e t_{\mathrm{ELM}} \sim \nu_e \tau_i = \sqrt{m_i/m_e}\ \nu\tau$ is not necessarily small, implying a potentially significant impact of the BGK collision term on the electron dynamics. We also note that, still using the estimates of [18], the electron–ion temperature relaxation rate scales as $\nu_{ei} \sim \sqrt{m_e/m_i}\ \nu_i \sim (m_e/m_i)\nu_e$, which justifies the fact that it is neglected in the present model. In summary, we have for the various collision processes, in order of importance:

- $t_{\mathrm{ELM}}\ \nu_{ei} \sim \sqrt{m_e/m_i}\ \nu\tau$,
- $t_{\mathrm{ELM}}\ \nu_i \sim \nu\tau$,
- $t_{\mathrm{ELM}}\ \nu_e \sim \sqrt{m_i/m_e}\ \nu\tau$,

with the scaling $\nu_{ei} \ll \nu_i \ll \nu_e$.

When applicable, the simulation results will be compared to the free-streaming model [11, 12]. Using a perturbative approach, we extended this analytical model to include first-order corrections arising from the ion–ion collision operator (the procedure is briefly sketched in the appendix). In contrast, in the full Vlasov simulations both the *direct* effect of the ion–ion collisions and the *indirect* effect of the electron–electron collisions (mediated by the electric field) contribute to modify the ion fluxes on the walls.

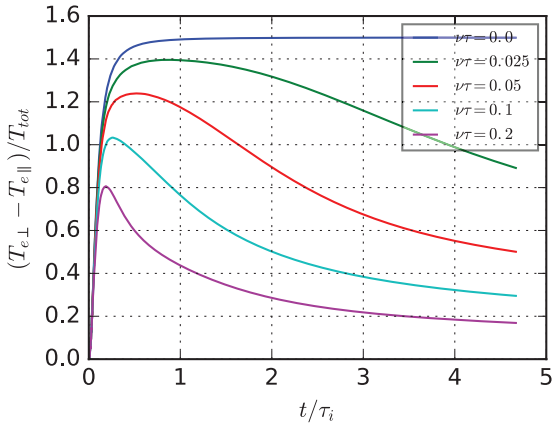

Figure 4. Electron temperature anisotropy $T_{\perp,e} - T_{\parallel,e}$ normalized to the total temperature.

3. Simulation results with impulse source

In this section, we report on simulation results for the case of an impulse response $s(t) = \delta(t)$, i.e. the limit case for which the ELM plasma is created instantaneously. This situation lends itself well to comparisons with the modified free-streaming model with first-order collisional corrections described in the appendix.

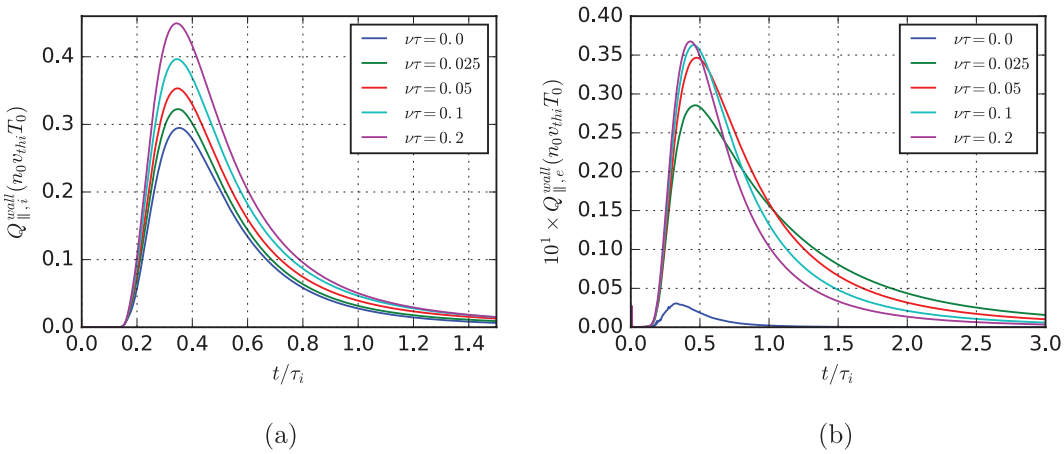

Figure 5. Temporal evolution of the ion (a) and electron (b) parallel energy fluxes at the right wall $x = L$. (a) H^+. (b) e^-.

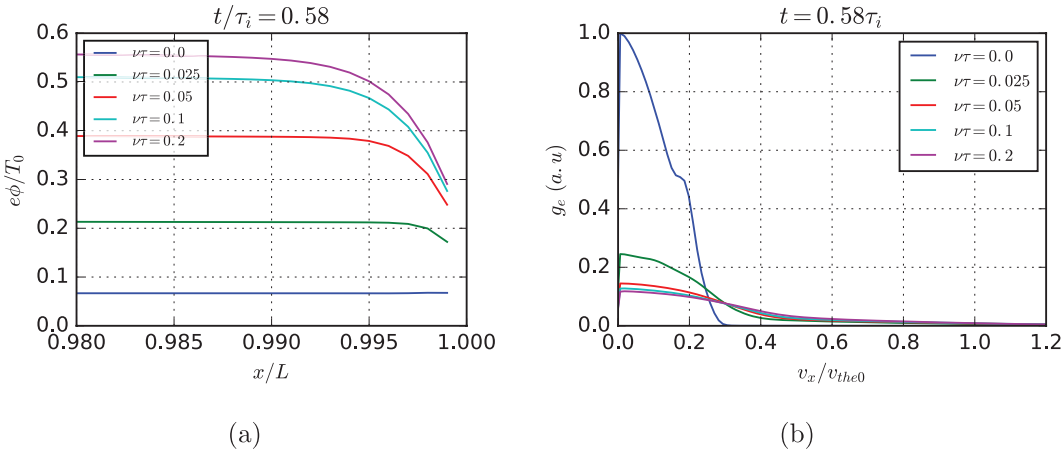

Figure 6. (a) Electric potential profile near the wall at $t = 0.58\tau_i$. (b) Electron parallel velocity distribution function at the target plate $x = L$ at $t = 0.56\tau_i$. All distributions are normalised to the peak value of the distribution for the $\nu\tau = 0$ case.

3.1. Particle fluxes at the target plate

After the ELM plasma is created at the centre of the computational box ($x = 0$), it starts expanding along the parallel direction until it reaches the divertor plates. The typical temporal profile of the particle flux at the wall features a steep growth phase followed by a much slower decay. This behaviour is captured quite well by the modified free-streaming model (with c_S replacing $v_{th,i}$) [11]. Here, we want to assess the impact of isotropising collisions on this behaviour.

The ion particle flux $j_i = \int g_i v_x \mathrm{d}v_x$ is shown in figure 1(a) for different values of the collisionality, quantified by the parameter $\nu\tau$. Although the general shape of the curve is the same, the peak exhibits a slight increase (up to 9% for $\nu\tau = 0.2$) with growing collisionality. The time at which the peak occurs decreases with growing $\nu\tau$ with a reduction of about 4% at most.

Figure 1(b) shows the ion particle flux predicted by the modified free-streaming model. The agreement is excellent in the collisionless case $\nu\tau = 0$. However, the collisions seem to have virtually no effect on the ion particle flux, which increases by less than 1% with increasing $\nu\tau$ (see inset). This is an interesting finding because it confirms that the direct impact of ion–ion collisions (the only type included in the collisional free-streaming model) on the ion flux is actually negligible. Thus, most of the increase observed in the Vlasov simulations (figure 1(a)) is due to the indirect effect of electron–electron collisions. The electron particle flux (not shown here) is slightly higher than the ion one and exhibits the same dependency on $\nu\tau$.

Let us now try to understand this behaviour in more detail. Due to the shortness of the ion transit time in the Debye sheath that may form in front of the wall, the ion particle flux can be considered as nearly constant inside the sheath. As a consequence, the observed variation of the ion particle flux with $\nu\tau$ must be related to energy transfer in the bulk plasma during the initial quasi-neutral expansion, before it reaches the wall. For this reason, it is relevant to look at the plasma temperatures at the centre of the domain ($x = 0$), shown in figures 2 and 3.

As can be expected from the smallness of $\nu_i\tau_i$, the ion temperatures (figure 2) are only mildly affected by the collisions in the time range occurring before the maximum flux is received on the plates, i.e. $t \lesssim 0.5\tau_i$. For the electrons the situation is quite different (figure 3). Starting from an isotropic distribution $T_{\parallel,e} = T_{\perp,e}$, the electron parallel temperature initially drops due to the quasi-neutral plasma expansion. In the collisionless case, due to the adiabaticity of the expansion (most of the electrons are trapped in a slowly expanding potential

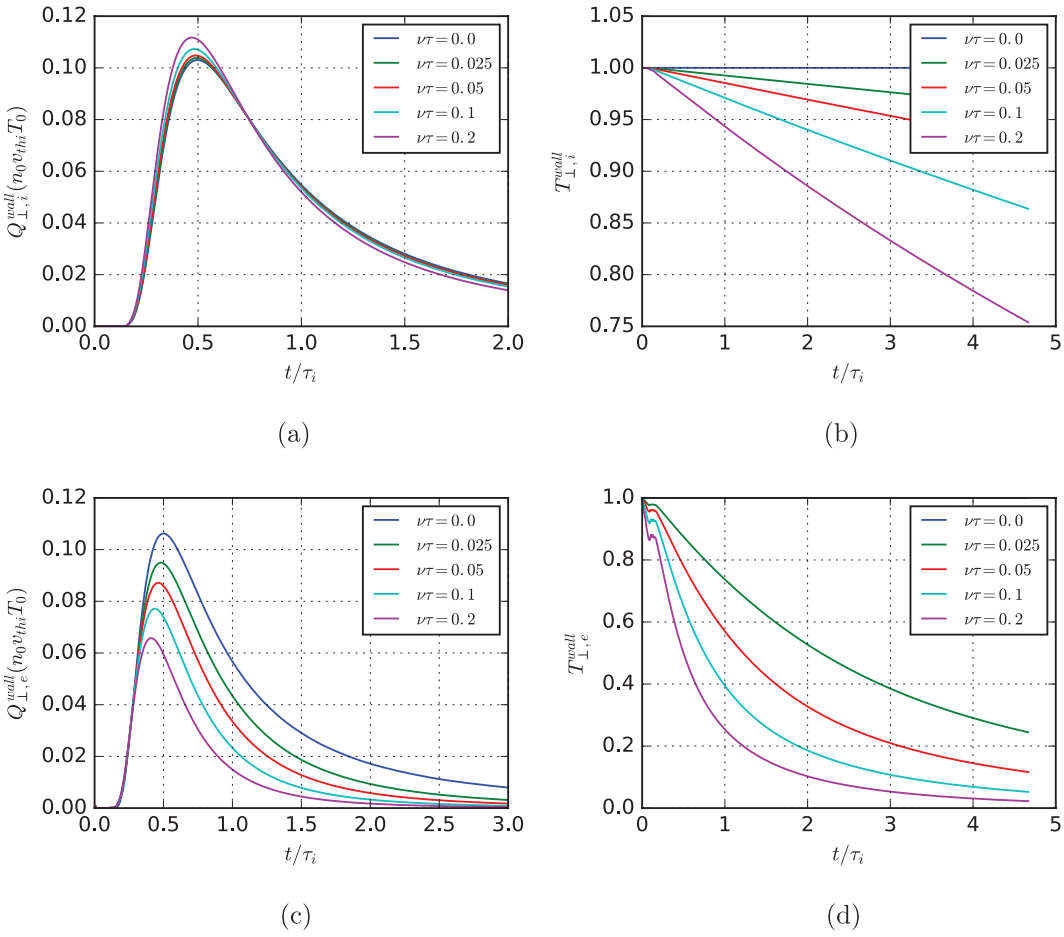

Figure 7. Temporal evolution of the perpendicular energy fluxes (left frames) and perpendicular temperatures (right frames) at the right plate $x = L$, for ions (top) and electrons (bottom). (a) H^+, (b) H^+, (c) e^-, (d) e^-.

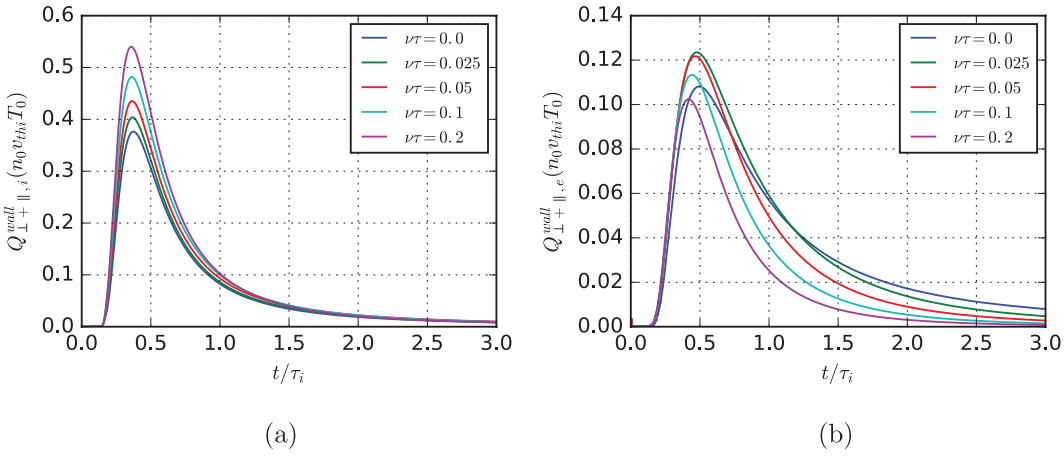

Figure 8. Ion (a) and electron (b) total energy fluxes $Q^{\text{wall}}_{\perp+\parallel}$ at the right plate $x = L$. (a) H^+, (b) e^-.

well) and quasi-neutrality, the electron parallel temperature follows the ions'. Using the free-streaming temperature evolution [11], one obtains $T_{\parallel}(t) \sim [1 + (t/\tau_\sigma^2)]^{-1}$, so that the parallel temperature decays over a time $\tau_\sigma = \sigma_0/c_{S0} \ll \tau_i$. Around such timescale τ_s the electron temperature anisotropy is maximum (figure 4). For later times, electron–electron collisions start playing a role, transferring energy from the perpendicular to the parallel motion, so that the temperature anisotropy decreases again. The net effect is a slowing down of the electron parallel temperature decay (figure 3(a)) compared to the collisionless case. Thus, the evolution of the electron parallel temperature is governed by the competition between adiabatic cooling (due to the parallel expansion) and collisional heating (due to exchanges with the perpendicular temperature bath).

Part of the energy that goes from $T_{\perp,\text{e}}$ to $T_{\parallel,\text{e}}$ contributes to accelerating the electrons in the parallel direction. This,

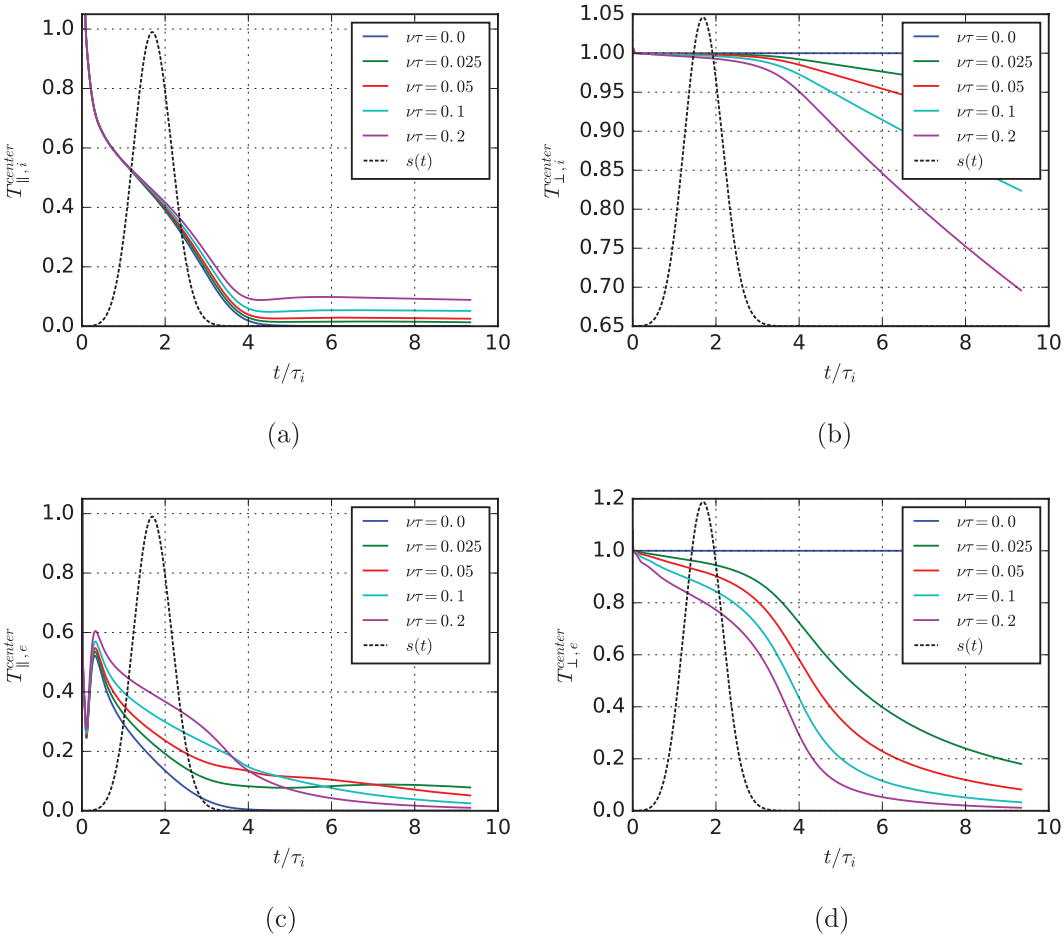

Figure 9. Evolution of the temperatures for the ions (top frames) and the electrons (bottom frames) at the center of the domain ($x = 0$) for a time-distributed source. Left frames: parallel temperatures; right frames: perpendicular temperatures. For clarity, the profile of $s(t)$ (in arbitrary units) is shown on each plot. (a) H^+, (b) H^+, (c) e^-, (d) e^-.

because of quasi-neutrality, accelerates in turn the ions and contributes to the increased ion particle flux observed in figure 1. In summary, the enhanced ion particle flux is due to: (i) a (collisional) energy transfer from $T_{\perp,\mathrm{e}}$ to $T_{\parallel,\mathrm{e}}$, followed by (ii) a (collisionless) transfer to the ions through the self-consistent electric field. The limited efficiency of this process is mainly due to the fact that the initial distribution is isotropic, and becomes anisotropic only after the initial adiabatic expansion in the parallel direction.

3.2. Energy fluxes at the target plate

In magnetic fusion devices, the energy flux sustained by the divertor plates is a crucial parameter and a thorough understanding of it is of vital importance for tokamak operation. Here, we investigate how the parallel and perpendicular heat fluxes are affected by isotropising collisions.

Let us first focus on the parallel energy flux $Q_{\parallel,s} = \frac{m_s}{2}\int v_x^3 f_s(\mathbf{v})\mathrm{d}^3\mathbf{v}$. For the ions, the free-streaming model predicts a negligible impact of ion–ion collisions on the flux (appendix). However, a rather strong dependency on $\nu\tau$ is observed in the numerical simulations (figure 5(a)), with a relative variation of the peak flux up to 50% for $\nu\tau = 0.2$ compared to the collisionless case. This is much larger than the variation observed for the ion particle flux (see figure 1(a)). Thus, the mechanism evoked for the particle flux (energy transfer from the perpendicular to the parallel ion motion, followed by a transfer to the ions through the electric field) cannot explain the entire variation observed in figure 5(a). Remember that such transfers occur during the initial adiabatic quasi-neutral expansion: the sheath has no influence on them, because the particle fluxes are conserved inside the sheath. This is not true, however, for the energy fluxes, so part of the observed flux increase may come from acceleration in the sheath. Using a stationary sheath approximation, the energy flux through the sheath increases of a quantity $\Delta Q_\parallel = Zej|\Delta\phi|$, where $e\Delta\phi \sim T_{\parallel,\mathrm{e}}$ is the potential drop in the sheath. In figure 6(a) we show the potential profile near the wall at $t = 0.58\tau_\mathrm{i}$. The sheath potential drop ranges from nearly zero in the collisionless case to about 0.25 T_0 for $\nu\tau = 0.2$. Using $Q_\parallel^{\mathrm{SE}} \approx \frac{m_\mathrm{i}}{2} j c_\mathrm{S}^2$ as an estimate of the flux at the sheath entrance (SE), the relative variation in the sheath can be estimated as $\Delta Q_\parallel / Q_\parallel^{\mathrm{SE}} = e\Delta\phi/T_0$. In our case, this would yield an increase in the ion heat flux of about 25% compared to the collisionless case for $\nu\tau = 0.2$, which is roughly consistent with figure 5(a). In summary, electron–electron isotropising collisions delay the cooling of the parallel electron temperature by feeding energy from the perpendicular distribution.

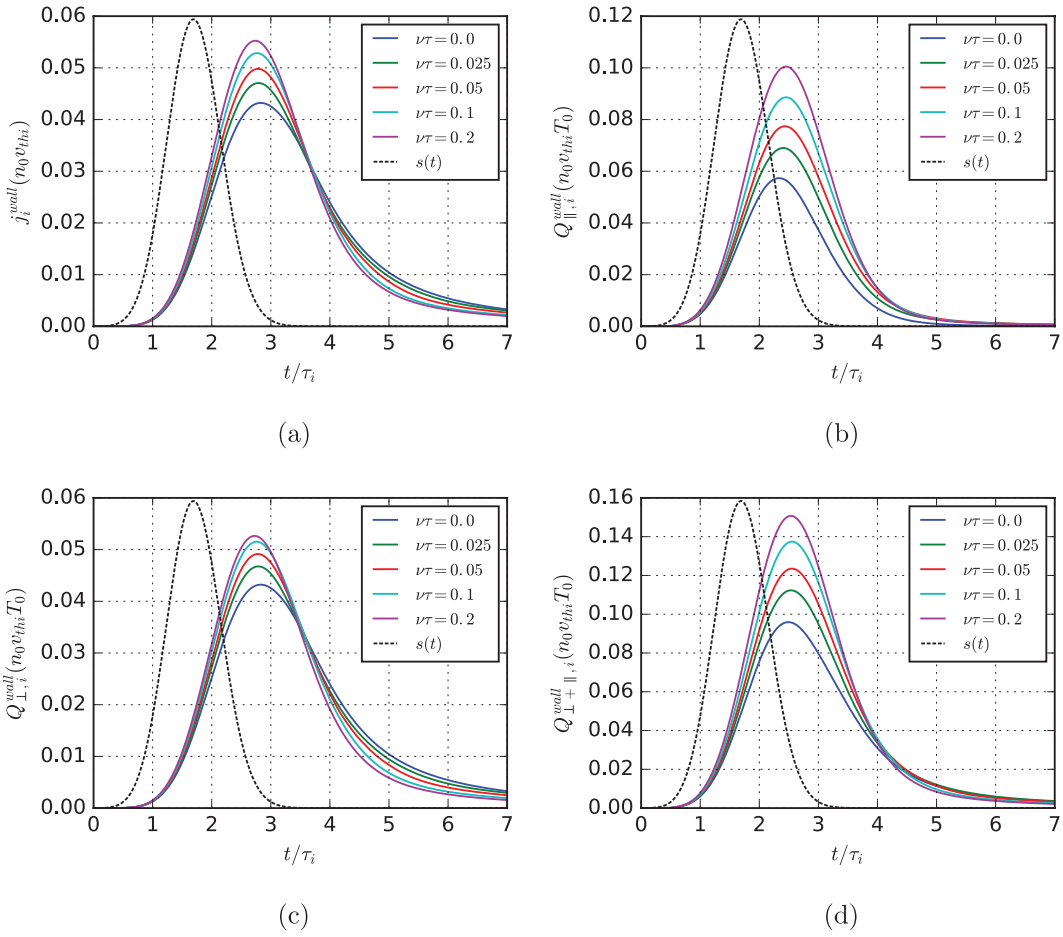

Figure 10. Ion fluxes at the target plate for a time-distributed source: (a) particle flux; (b) parallel energy flux; (c) perpendicular energy flux; (d) total energy flux. (a) H^+, (b) H^+, (c) H^+, (d) H^+.

Due to this increased parallel electron temperature a non-negligible sheath potential may persist at the time when the fluxes reach the wall, leading to an increased ion parallel energy flux.

Now let us examine the electron parallel energy flux (figure 5(b)). In the collisionless case, it is typically two orders of magnitude lower than the ion flux. The introduction of collisions induces a tenfold increase of the electron parallel energy flux, up to one tenth of the ion value. The large difference between the collisionless and collisional cases can be understood by looking at the electron velocity distribution function at the wall around the time when the fluxes are maximal (figure 6(b)). While the electron density at the wall decreases with $\nu\tau$ due to the increase of the sheath potential drop, a significant difference can be observed in the structure of the distribution. The velocity distribution is depleted in the collisionless case for $v > 0.3\ v_{the0}$, whereas a significant high-energy tail remains when collisions are present. This can be readily explained by the fact that, in the collisionless case, the higher energy electrons have already been lost to the wall in the very early stages of the expansion, well before the time corresponding to the peak plasma fluxes at the wall. In contrast, in the collisional cases, the electron parallel velocity tail is kept alive by the collisional transfer from the perpendicular to the parallel motion.

The peak electron parallel energy flux (figure 5(b)) increases quickly at small values of $\nu\tau$, then saturates at a constant level around $\nu\tau \approx 0.1$. This saturation has probably different causes. In part, it is due to the reduced efficiency of the perpendicular-to-parallel energy transfer for large $\nu\tau$, because the two temperatures equilibrate at an earlier time, so that the net transfer is limited. Another reason may be the formation of the Debye sheath (see figure 6(a)), which prevents the less energetic electrons from reaching the wall. The faster electrons, which can overcome the sheath potential, reach the plate well before the main plasma peak and thus do not contribute to figure 5(b).

The perpendicular energy flux $Q_{\perp,s} = j_s T_\perp$ shows little variation with collisionality for the ions (figure 7(a)). Indeed the (small) increase in j_i observed previously is mitigated by the (also small) decrease of $T_\perp$ (figure 7(b)). The situation is different for the electrons, for which a significant transfer from $T_\perp$ to $T_\parallel$ has occurred (figure 7(d)) resulting in a reduced flux with growing $\nu\tau$ (figure 7(c)). The wiggles visible on figure 7(d) are numerical fluctuations arising because the region near the wall is initially empty of plasma.

Adding up the parallel and perpendicular energy fluxes for each species (figure 8), we obtain a net increase with collisionality of the total energy deposition (time integral of the energy flux) for the ions. The electron total energy flux, about five times lower than the ions', increases for very small values

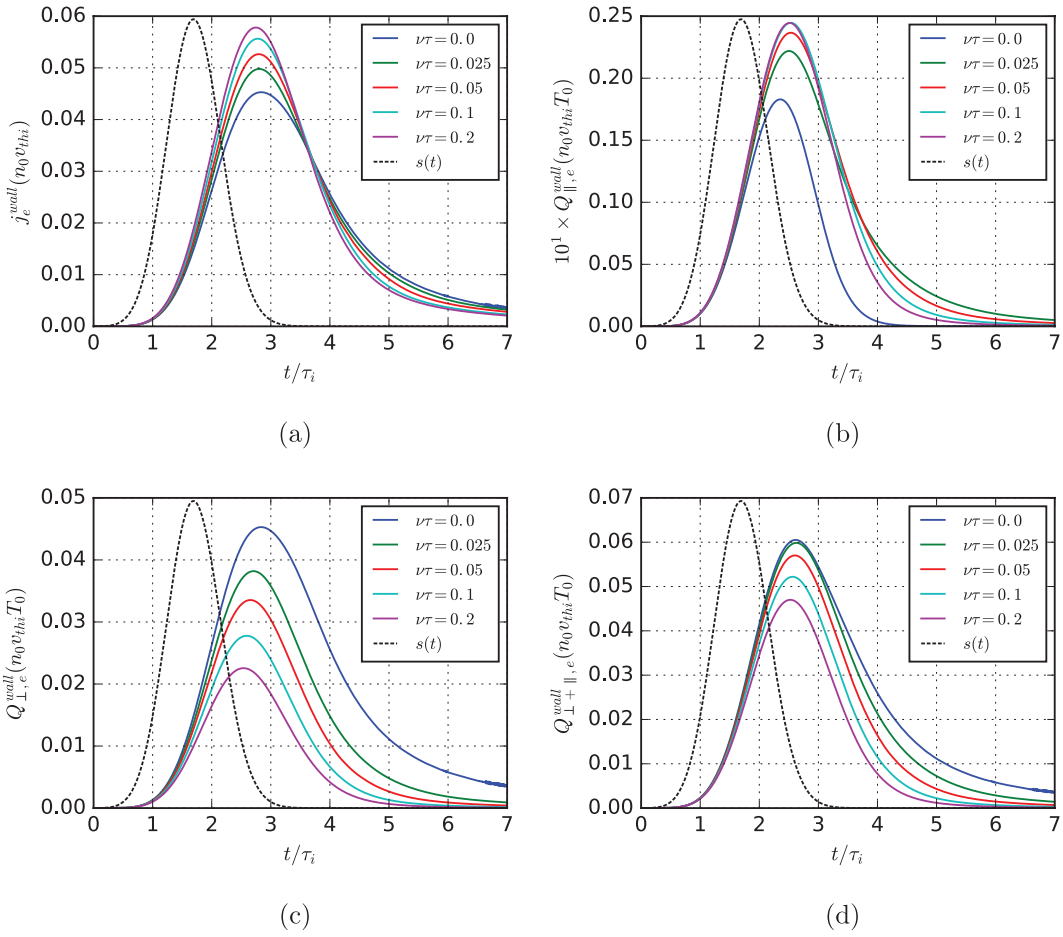

Figure 11. Electron fluxes at the target plate for a time-distributed source: (a) particle flux; (b) parallel energy flux; (c) perpendicular energy flux; (d) total energy flux. (a) e^-, (b) e^-, (c) e^-, (d) e^-.

of $\nu\tau$, then decreases again for larger collisional rates. The former behaviour is due to the rapid increase of the parallel flux with collisionality, while the subsequent decrease is governed by the perpendicular flux.

These results are in good agreement with those obtained with the 1D3V PIC code `BIT1`, as shown in figure 18 of [11], which show an increase of the ion energy flux and a decrease of the corresponding electron flux in the collisional case. In [11] the authors also provide an estimate (based on the values of $\nu_e\tau_i$) of the impact of isotropising collisions for an ITER scenario. Although the effect of collisions may well be smaller than what was observed in our simulations, it is nevertheless expected not to be negligible.

4. Simulation results with time-distributed source

We will now examine whether the previous observations persist when the plasma is injected at a finite rate using the source envelope $s(t)$ given by equation (11), with parameters $t_0 = 1.4\tau_i$, $\sigma_t = t_0/2 = 0.7\tau_i$, which peaks at $t_m = \sigma_t(1+\sqrt{2}) \approx 1.7\tau_i$. The duration of the source σ_t is about ten times longer than the characteristic timescale for the parallel expansion of the ELM burst $\tau_\sigma = \sigma_0/c_S$, so that the plasma state in the injection zone (around $x = 0$) may significantly

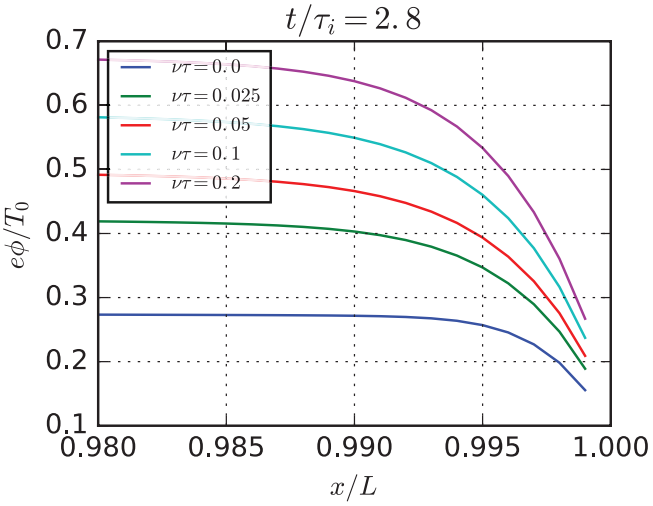

Figure 12. Electric potential profile near the wall at $t \approx 2.8\tau_i$ for a time-distributed source.

evolve during the injection. Therefore, seen from the perspective of the target plates, the plasma contained in this central region acts as an effective source, which may have different properties compared to the nominal parameters of the external source as specified above. In this respect, the ion and electron

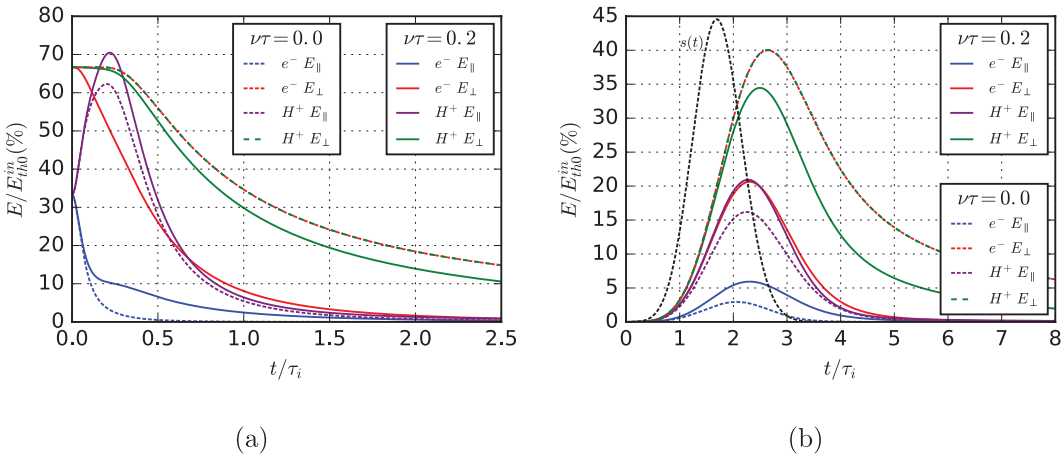

Figure 13. Temporal evolution of the parallel and perpendicular kinetic energies for ions and electrons, expressed as a percentage of the total injected energy per species $E^{in}_{\mathrm{th0}} = \frac{3T_0}{2}\int N(x)\mathrm{d}x \int s(t)\mathrm{d}t$: (a) impulse source; (b) time-distributed source. In each case we compare the collisionless case (dashed lines) with the $\nu\tau = 0.2$ collisional case (solid lines).

temperatures at the centre of the domain are a good indicator of the plasma state there.

Let us first consider the ion parallel temperature (figure 9(a)). The competition between plasma injection and the parallel expansion/cooling results in a lower effective bulk temperature (in the range 0.3–0.6T_0) during the injection time $0 < t \lesssim 3\tau_\mathrm{i}$. The variation of $T_{\parallel,i}$ between the various $\nu\tau$ values remains negligible and $T_{\perp,i}$ is essentially constant (figure 9(b)), confirming the low impact of ion–ion collisions in that case. The electron parallel temperature (figure 9(c)) is lower than the ion one (because energetic electrons can escape fast compared to the injection rate) and far more sensitive to collisional isotropisation, resulting in a decrease in $T_{\perp,\mathrm{e}}$ of up to 20% during the injection time (figure 9(d)). Note that the rapid change of $T_{\parallel,\mathrm{e}}$ in the very early injection stage is not physically significant and stems from the fact that the domain is initially empty of plasma, so that fluctuations dominate the calculation of $T_{\parallel,\mathrm{e}}$.

Considering now the fluxes at the target plate (figures 10 and 11), the introduction of a finite injection rate obviously leads to a spreading in time of the particle and energy deposition and consequently to reduced peak flows compared to the impulse response, the total energy and particle content being the same. The slower dynamics leaves more time for collisions to have an effect, so that the relative impact of the electron temperature isotropisation is similar in nature but enhanced in value compared to the case of impulse response. Also, the strong difference for the electron parallel energy flux between the collisionless and collisional case observed for the impulse response (figure 5(b)) is much reduced in the case of a time-distributed source (figure 11(b)). All in all, as in the the case of an impulse source, the total power load on the target plates is (moderately) increased by the effect of isotropising collisions

Finally, we show in figure 12 the potential profile in the vicinity of the target plate, around the time when the fluxes on the walls are maximum. As in the case of an impulse source, the sheath is much more prominent when collisions are included.

5. Energy transfer dynamics

As an illustration of the global energy transfer dynamics, we show in figure 13 the evolution of the parallel and perpendicular kinetic energies for each species, integrated over the whole simulation box, for both kinds of sources. We compare the collisionless case (dashed lines) with the most collisional one, $\nu\tau = 0.2$ (continuous lines).

Let us first concentrate on the collisionless impulse response (figure 13(a), dashed lines), which is easier to interpret. On very short time scales ($\sigma_0/v_{\mathrm{th,e}}$), the more mobile electrons escape from the injection region, leaving behind a positive charge and therefore a strong electric field. This electric field subsequently accelerates the ions and slows down the remaining electrons: this is reflected in the increase of the ion and decrease of the electron parallel energies. During this phase the plasma undergoes an adiabatic quasi-neutral expansion. At a time of the order of the transit time $\tau_L = L/c_{\mathrm{S0}} = \tau_\mathrm{i}/\sqrt{2}$ both species begin to reach the target plates and leave the domain. This is signalled by the plateaus in the perpendicular energies, which start decaying at around $0.25\tau_\mathrm{i}$. The parallel energies also drop after that time.

When one considers the effect of isotropising collisions on this scenario, one notices several effects (figure 13(a), solid lines):

(i) The electron parallel energy decays less rapidly. This is because of the collisional transfer from the perpendicular to the parallel temperature described in section 3.1.

(ii) Concomitantly, the ion parallel energy increases more than in the collisionless case, because the extra electron parallel energy is partly converted into ion parallel energy through the electric field. See again section 3.1.

(iii) The ion perpendicular energy is little affected by the collisions and starts decreasing only when the ions reach the target plate.

(iv) The electron perpendicular energy decays much faster than the corresponding ion energy (because $\nu_\mathrm{e} \gg \nu_\mathrm{i}$) through heat exchange with the electron parallel temperature bath, which is much colder because of the adiabatic expansion.

The chronology of the various transfers is no more readily visible in the case of the time-distributed source, because the competing effects of plasma injection, collisional or electrostatic energy transfers, and wall losses, all occur simultaneously. Nevertheless, we still observe a strong decrease of the electron perpendicular energy, together with an increase of both ion and electron parallel energies.

6. Conclusions

In this paper, we extended a previously developed model [10] for parallel transport in the scrape-off layer following an ELM event. The earlier model ignored the perpendicular dynamics and assumed that the perpendicular velocity distribution is a Maxwellian with constant temperature. Here, we relaxed the latter hypothesis and let the perpendicular temperature evolve self-consistently in time, although the distribution is still supposed to be Maxwellian. The resulting model is governed, for each particle species, by a kinetic Vlasov equation in the parallel direction coupled to a fluid equation for the perpendicular temperature. In this work, we reported on the first results obtained with this model.

The most important result was to confirm that, while ion–ion collisions have an almost negligible effect, the impact of the electron–electron collisions can be quite significant on the various fluxes, both for electrons and ions. The dominant effect stems from the electron–electron temperature isotropisation, which transfers electron thermal perpendicular energy to the parallel motion. Part of this energy goes into heating the electrons in the parallel direction; another part is transferred to the ions through acceleration by the self-consistent electric field. This transfer occurs during the initial quasi-neutral plasma expansion (where it is analogous to inducing an increased effective sound speed) and also in the Debye sheath, whose depth and width increase with collisionality. The net result is an increase of the peak values of the ion particle and energy fluxes at the target plate, while the total electron energy flux decreases. All in all, the peak power load increases of about 30%, as can be seen from figures 8, 10(d) and 11(d). The balance between the ionic and the electronic energy fluxes is also changed compared to the collisionless case. Indeed, while the ion flux increases through the energy transfer mechanisms described above, the electron flux first increases at low collisionality (thanks to the perpendicular to parallel transfer in the quasi-neutral expansion) but then saturates at higher collisionality. Thus, the relative importance of the electrons in the energy fluxes is reduced by the collisions.

In summary, we constructed a hybrid model (kinetic in the parallel direction and fluid in the perpendicular plane) that can treat the parallel transport in the scrape-off layer, including the effect of temperature anisotropy, in the framework of a 1D1V phase space. The model reproduces, at a much lower computational cost, some of the results obtained with a 1D3V PIC code [11] and thus constitutes a useful tool to study energy deposition on the divertor plates following an ELM event.

Several further improvements on the present model can be envisioned. First, a more sophisticated collision operator (e.g. Fokker–Planck or Lenard–Balescu) could be used in place of the BGK term employed here. Electron-ion collisions, which were neglected here, may also be included. Second, perpendicular drifts should also be taken into account. This would lead to a complete set of fluid equations (continuity, momentum, and energy) for the perpendicular dynamics, instead of the single temperature equation used so far. In this context, perpendicular diffusion may also be added through appropriate transport coefficients. Finally, neutral particle dynamics near the divertor could also be included in an extension of the present model.

Acknowledgments

The authors acknowledge the support of the French Agence Nationale de la Recherche (ANR), project PEPPSI, reference ANR-12-BS09-028-01. We thank Claudia Negulescu for several useful discussions on the hybrid model.

Appendix. Free-streaming model with first-order collisional corrections

The model presented herein extends the free-streaming model of [7, 11, 12]. Taking advantage of the relative smallness of the collisional rates for the ion dynamics, we develop a perturbative analysis of the field-free collisional ion dynamics. In the particular case of a Gaussian spatial envelope and impulse time source, first order corrections to the ion moments can be obtained for a negligible numerical cost.

For brevity we will sketch the principle of the analysis in a quite general way, but present detailed calculations only for the case of an impulse source $s(t) = \delta(t)$ and the envelopes $N(x)$ and $G(v)$ used throughout this paper (equations (8)–(9)). In that particular case, closed analytical forms can be obtained easily for the collisionless free-streaming model and simple expressions can be given for the first order collisional corrections.

The starting point of the analysis is the integral form of the hybrid model for $(g, T_\perp)$

$$g(t,x,v) = \int_0^t \mathrm{e}^{\nu(t'-t)} s(t') N(x + v(t'-t)) G(v) \mathrm{d}t' + \nu \int_0^t \mathrm{e}^{\nu(t'-t)} g_{\mathrm{M}}(t', x + v(t'-t), v) \mathrm{d}t' \tag{A.1}$$

$$T_\perp(t,x) = T_{\perp 0} \mathrm{e}^{-\frac{\nu t}{3}} + \frac{\nu}{3} \int_0^t \mathrm{e}^{\frac{\nu(t'-t)}{3}} T_\parallel(t', X_u) \mathrm{d}t' + \int_0^t \mathrm{e}^{\frac{\nu(t'-t)}{3}} \frac{s(t') N(X_u)(T_{\perp 0} - T_\perp(t', X_u))}{n(t', X_u)} \mathrm{d}t' \tag{A.2}$$

where $X_u = X_u(t', t, x)$ is a solution of $\mathrm{d}X_u/\mathrm{d}t' = u_x(t', X_u)$ and $X_u(t,\ t,\ x) = x$ is a characteristic curve of the perpendicular temperature equation. Considering times such that $\nu t \ll 1$, all quantities in the system (A.1)–(A.2) can be expanded in a Hilbert series in $\epsilon \equiv \nu t$. For instance, for the distribution function we have: $g = g^0 + \epsilon g^1 + \ldots$. This procedure yields an infinite system of equations where each order is coupled with the

previous ones. Note that the superscripts '0', '1', etc refer to the orders of the Hilbert expansion, whereas the subscript '0' refers to the properties of the ELM source.

Now we consider the impulse response, i.e. $s(t) = \delta(t)$. Up to the first order, such expansion yields the system

$$g^0(t,x,v) = N(x - vt)G(v),$$
$$tg^1(t,x,v) = -tg^0(t,x,v) + \int_0^t g^0_{\mathrm{M}}(t', x + v(t'-t), v)\mathrm{d}t'. \tag{A.3}$$

Thanks to the fact that both $N(x)$ and $G(v)$ are both Gaussian functions and to the linearity in (x, v) of the characteristics, the free-streaming solution g^0 can be written as a drifting Maxwellian

$$g^0(t,x,v) = \frac{\sigma_0 \exp\left[-\frac{x^2}{2\sigma_2^0(t)}\right]}{\sqrt{\sigma_2^0(t)}} \frac{\exp\left[-\frac{m_i(v-u^0(t,x))}{2T_\parallel^0(t)}\right]}{\sqrt{2\pi T_\parallel^0(t)}}, \tag{A.4}$$

with $\sigma_2^0(t) = \sigma_0^2[1 + (t/\tau_\sigma)^2]$, $\tau_\sigma = \sigma/v_{\mathrm{th},i0}$, $T_\parallel^0(t) = T_{\parallel 0}[1 + (t/\tau_\sigma)^2]^{-1}$ and $u^0(t,x) = v_{\mathrm{th},i0}\frac{x}{\sigma_0}\frac{t/\tau\sigma}{1+(t/\tau_\sigma)^2}$.

All parallel velocity moments of g^0 can be readily computed from those quantities. At this order, both the distribution function and its parallel moments can be obtained in the case of an arbitrary source by mere convolution of the source with the impulse response. Due to the spatially uniform initial condition for $T_\perp$, we have at the lowest order the constant solution: $T_\perp^0(t,x) = T_{\perp 0}$. Thus the total temperature required to build the isotropic Maxwellian term at the next order has the simple form $T^0(t) = \frac{1}{3}[2T_{\perp 0} + T_\parallel^0(t)]$. Using the explicit forms of the zeroth order moments and thanks to their particularly simple form for $s(t) = \delta(t)$, the integrand $g^0_{\mathrm{M}}(t', x + v(t'-t), v)$ can also be recast as a drifting Maxwellian

$$g^0_{\mathrm{M}}(t', x + v(t'-t), v) = \frac{\exp\left[-\frac{x^2}{2\sigma_{2M}(t',t)}\right]}{\sqrt{\sigma_{2M}(t',t)}} \frac{\exp\left[-\frac{m_i(v-u_{\mathrm{M}}(t',t,x))}{2T_{\mathrm{M}}(t',t)}\right]}{\sqrt{2\pi T_{\mathrm{M}}(t',t)}}, \tag{A.5}$$

with

$$T_{\mathrm{M}}(t',t) = \frac{T^0(t')}{(\frac{t'-t}{\tau_\sigma})^2 \frac{\sigma_0^2}{\sigma_2^0(t')}\frac{T^0(t')}{T_{\parallel 0}} + \left[1 - \frac{t'(t'-t)}{\tau_\sigma^2(1+t'^2)}\right]^2}, \tag{A.6}$$

$$\sigma_{2M}(t',t) = \sigma_2^0(t')\frac{T^0(t')}{T_{\mathrm{M}}(t',t)}, \tag{A.7}$$

$$u_{\mathrm{M}}(t',t,x) = -\frac{v_{\mathrm{th},i0}\,x}{\sigma_2^0(t')}\frac{T_{\mathrm{M}}(t',t,x)}{T^0(t')}\left[\left(\frac{(t'/\tau_\sigma)^2}{1+(t'/\tau\sigma)^2}\frac{t'-t}{\tau_\sigma}\right) - \frac{t}{\tau_\sigma}\frac{T^0(t')}{T_{\parallel 0}}\right]. \tag{A.8}$$

With the above expressions, the parallel velocity moments of the integrand in equation (A.3) can be expressed. First-order corrections to the parallel velocity moments (particularly the collisional correction to the parallel temperature $T_\parallel^1$) are then obtained by numerical time integration.

For the perpendicular temperature, expanding equation (A.2) to first order in νt and neglecting the transport term due to the absence of any spatial dependence of the temperatures at zeroth order, we obtain:

$$tT_\perp^1 = -\frac{t}{3}T_\perp^0 + \int_0^t \frac{1}{3}T_\parallel^0(t')\mathrm{d}t' = \frac{1}{3}\left[T_{\parallel 0}\tau_\sigma \arctan\left(\frac{t}{\tau_\sigma}\right) - tT_\perp^0\right], \tag{A.9}$$

so that

$$T_\perp(t) = T_{\perp 0}(1 - \frac{\nu t}{3}) + T_{\parallel 0}\frac{\nu\tau_\sigma}{3}\arctan\left(\frac{t}{\tau_\sigma}\right). \tag{A.10}$$

In summary, we have developed an analytical approach that extends the original free-streaming model [7] to include first-order collisional corrections. For the range of $\nu\tau$ values considered here, these first-order effects can be summarized as follows:

- A slight increase in the peak values of the particle (up to 1%) and energy (up to 4–5%) ion fluxes on the wall;
- A reduction of the perpendicular temperature (less than 3% at the time when the wall fluxes are maximal) and an increase of the parallel temperature. At the time when the wall fluxes are maximum, the parallel temperature is already quite low, and consequently the relative increase in parallel temperature is large (around 50%) although the absolute energy transfer is small compared to the initial energy.

Note that these values significantly underestimate the variations obtained with the full model, where the main factor is the energy transfer between electrons and ions via the self-consistent electric field, which is neglected in the free-streaming model.

References

[1] Janeschitz G and ITER JCT an HTs 2001 *J. Nucl. Mater.* **290–3** 1

[2] Behrisch R, Federici G, Kukushkin A and Reiter D 2003 *J. Nucl. Mater.* **313–6** 388

[3] Wiesen S, Brezinsek S, Jarvinen A, Eich T, Fundamenski W, Huber A, Parail V, Corrigan G, Hayashi N and JET EFDA Contributors 2011 *Plasma Phys. Control. Fusion* **53** 124039

[4] Pamela S J P, Huysmans G T A, Beurskens M N A, Devaux S, Eich T, Benkadda S and JET EFDA Contributors 2011 *Plasma Phys. Control. Fusion* **53** 054014

[5] Pamela S *et al* and JET Contributors 2016 *Plasma Phys. Control. Fusion* **58** 014026

[6] Havlikova E, Fundamenski W, Tskhakaya D, Manfredi G and Moulton D 2012 *Plasma Phys. Control. Fusion* **54** 045002

[7] Fundamenski W, Pitts R A and JET EFDA Contributors 2006 *Plasma Phys. Control. Fusion* **48** 109

[8] Tskhakaya D, Subba F, Bonnin X, Coster D P, Fundamenski W, Pitts R A and JET EFDA Contributors 2008 *Contrib. Plasma Phys.* **48** 89–93

[9] Tskhakaya D, Pitts R A, Fundamenski W, Eich T, Kuhn S and JET EFDA Contributors 2009 *J. Nucl. Mater.* **390–1** 335–8
[10] Manfredi G, Hirstoaga S and Devaux S 2011 *Plasma Phys. Control. Fusion* **53** 015012
[11] Moulton D, Ghendrih P, Fundamenski W, Manfredi G and Tskhakaya D 2013 *Plasma Phys. Control. Fusion* **55** 085003
[12] Moulton D, Fundamenski W, Manfredi G, Hirstoaga S and Tskhakaya D 2013 *J. Nucl. Mater.* **438** S633–7
[13] Shi E L, Hakim A H and Hammett G W 2015 *Phys. Plasmas* **22** 022504
[14] Guillemaut C *et al* 2015 *Plasma Phys. Control. Fusion* **57** 085006
[15] Guillemaut C *et al* and JET contributors 2016 *Phys. Scr.* **2016** 014005
[16] Aliev Y M and Silin V P 1963 *Nucl. Fusion* **3** 248
[17] Ichimaru S and Rosenbluth M N 1970 *Phys. Fluids* **13** 2778–9
[18] Dong C, Ren H, Cai H and Li D 2013 *Phys. Plasmas* **20** 102518
[19] Schekochihin A A, Parker J T, Highcock E G, Dellar P J, Dorland W and Hammett G W 2016 *J. Plasma Phys.* **82** 905820212
[20] Bhatnagar P L, Gross E P and Krook M 1954 *Phys. Rev.* **94** 511–25
[21] Filbet F, Sonnendrucker E and Bertrand P 2001 *J. Comput. Phys.* **172** 166–87
[22] Leveque R J 2002 *Finite Volume Methods for Hyperbolic Problems* (Cambridge: Cambridge University Press)